Journal of
Ship&Ocean
Technology
©JUNE 2001

SOTECH Vol. 5, No. 2, pp. 27~49, 2001

Comparison of Turbulence Models for the Prediction of Wakes around VLCC Hull Forms

Wu-Joan Kim[1], Do-Hyun Kim[1] and Suak-Ho Van[1]

[1]Marine Transportation Systems Division, Korea Research Institute of Ships and Ocean Engineering, Taejon, Korea; E-mail: wjkim@kriso.re.kr

Abstract

Turbulent flow calculations are performed for the two modern practical VLCCs with the same forebody and the slightly different afterbody, i.e. KVLCC and KVLCC2. Three k-ϵ turbulence models are tested to investigate the differences caused by the turbulence models. The calculated results around the two VLCC hull forms using O-O grid topology and profile-fitted surface meshes are compared to the measured data from towing tank experiment. The realizable k-ϵ model provided realistic wake distribution with hook-like shape, while the standard and RNG-based k-ϵ models failed. It is very encouraging to see that the CFD with relatively simple turbulence closure can tell the difference quantitatively as well as qualitatively for the two hull forms with stern frameline modification.

Keywords: turbulence model, stern hull form, realizable k-ϵ, grid topology

1 Introduction

In the initial stage of hull form design, it is customary to develop a new hull form based on a parent ship. Thus, it is essential for a designer to get enough information on changes of the flow characteristics due to the hull form variation. Traditionally towing tank tests have been carried out for the performance prediction of commercial ships such as tanker, bulk carrier and container ship. However, it usually takes several months and costs lots of money. Recently some shipyards are trying to utilize Computational Fluid Dynamics (CFD) for the performance prediction during the initial hull form design. It is very probable that the application of CFD as a colander, can reduce the number of model tests required for the hull form optimization. However, before declaring that CFD is a useful tool, it should be confirmed that it can tell the difference of flow characteristics due to the amount of hull form change as much as typically made in the shipyards. Another important issue to point out is that the users in ship yards are not familiar with the details of computational methods, stating that the numerical methods should be robust. Furthermore, CFD tools should provide the results within short period of time, since ship yards usually allow to get the results overnight. There have been several workshops on viscous flow around a ship(Larsson et al 1991, CFD Workshop Tokyo 1994, Himeno et al 1998). For the workshops, relatively simple hull forms without any bulbs such as HSVA/Dyne tanker and Series 60 models were used for the validation of the numerical methods and turbulence models. However, the hull forms used in those experiments are quite different from the modern hull forms of actual ships today. For better understanding of

the flow around a modern ship, it is necessary to validate the computational modeling against the reliable experimental data of practical commercial hull forms. In the present study turbulent flow calculations are performed for the two modern practical VLCCs with the same forebody and the slightly different afterbody(i.e., KRISO 300K VLCC F1+A1, F1+A2). The Reynolds-averaged Navier-Stokes equations for turbulent flows around model ships are solved using the cell-centered finite-volume schemes with several variation of the k-ϵ turbulence model. Two-equation model like k-ϵ model is still cost-effective to be used for design purpose. Furthermore, the so-called Launder and Spalding's wall function is utilized to bridge the fully turbulent region and the wall to save computational efforts. Kim et al.(1998) tested various turbulence models with wall function, showing the possibility of application to ship flow calculation. For the calculation, hull surface is depicted as a spline net, where bow and stern profiles are considered as grid lines with the same indices. Field grid system with O-O topology is generated using the solution of three-dimensional Poisson equation and trans-finite interpolation. The calculated results around the two VLCC hull forms are compared to the measured data from towing tank experiment. In the followings the details of computational modeling and calculated results are described. It is interesting to see that the CFD with relatively simple turbulence closure can tell the difference quantitatively as well as qualitatively for the two hull forms with stern frameline modification.

2 Hull Forms and Experiments

To confirm the capability of CFD as a design tool, two VLCC hull forms are chosen with the same forebody and slightly different afterbody. At first, a 300K VLCC hull form(F1+A1, namely, KVLCC) was designed and experiments were performed. Later, another 300K VLCC hull form(F1 + A2, namely, KVLCC2) with the same forebody and different afterbody was tested. The second one(KVLCC2) has more U-shaped stern frame lines, as shown in Fig.1. The principal particulars of the test ships are given in Table 1. Two model ships of KRISO VLCCs with the scale ratio of 1/58, are made of wood. Turbulence stimulators are studded at 19 station and at the middle of bow bulb with 10 mm interval, so as to make sure that the flow becomes fully turbulent afterwards. The details of measurement device, techniques and the uncertainty analysis results are already reported in other papers(Van et al 1998). Thus, in the present paper, only the brief descriptions are given. The experiments were carried out in the towing tank of Korea Research Institute of Ships and Ocean Engineering(KRISO). The model ship is fixed at the towing carriage by using two clamping devices for local mean velocity measurements, in order to prevent the difficulties in positioning the probes in the experiments and in computing the flow for validation. However, the resistance tests were performed in the free condition, since towing force measurement is not very accurate in the fixed condition. It is believed that the difference of resistance performance between the fixed and free condition is very small for the present VLCC hull forms. For the local measurement of three-dimensional velocity field around the stern region, a 5-hole Pitot tube rake was utilized. However, local flow angles sometimes were out of calibration range of $\pm 40^o$ of pitch and yaw angles, especially just behind a stern cap or transom. In case that the local flow angle is out of calibration range, the measured data was discarded and velocity components could not be determined. For both ships, the stern cap of semi-sphere was attached to prevent the abrupt change at the end of stern bossing. Thus, the propeller plane(St. 0.35) is located just behind the stern cap. The propeller diameter is 9.8 m. The shaft center line of the VLCC is located at 5.8 m

Table 1: Principal particulars of test ships(KRISO 300K VLCC)

Ship Name	F1+A1(KVLCC)		F1+A2(KVLCC2)	
Designation	Ship	Model	Ship	Model
Scale ratio, λ	58.0			
Design speed	15.5 knots	1.047 m/sec	15.5 knots	1.047 m/sec
Length B.P., $L_{PP}(m)$	320.0	5.5172	320.0	5.5172
Breadth, $B(m)$	58.0	1.00	58.0	1.00
Draft, $T(m)$	20.8	0.3586	20.8	0.3586
Wetted surface area $S(m^2)$	27320.0	8.1213	27194.0	8.0838
Rudder area $Sr(m^2)$	273.3	0.0812	273.3	0.0812
Displacement volume $\nabla(m^3)$	312737.5	1.6029	312621.7	1.6023
Block coefficient C_B	0.8101		0.8098	

above the base line(i.e., $\frac{Z}{L_{pp}} = -0.04688$ from calm free surface). The measured mean velocity components at the propeller plane of the 300K VLCC models are compared in Fig. 2. The shape of wake contours are not much different since the hull form variation is not so great. However, it is observed that wake contours are more of circular shape and have stronger hook for KVLCC2. For details of wake distribution will be discussed later along with calculated results.

3 Governing Equations

The governing equations for turbulent flow in the present study are Reynolds-averaged Navier-Stokes equations for momentum transport and the continuity equation for mass conservation. The Cartesian coordinates are used, where (x, y, z) denotes downstream, starboard, and upward direction, respectively. The origin of the coordinates is located at the midship and calm free surface. All the quantities are non-dimensionalized by ship speed (V), length (L_{pp}) and fluid density (ρ).

Continuity equation

$$\frac{\partial u_k}{\partial x_k} = 0 \tag{1}$$

Momentum transport equation

$$\frac{\partial u_i}{\partial t} + \frac{\partial (u_i u_j)}{\partial x_j} = -\frac{\partial p}{\partial x_i} + \frac{\partial \tau_{ij}}{\partial x_j} \tag{2}$$

where $u_i = (u, v, w)$ are velocity components in $x_i = (x, y, z)$ directions, while p is static pressure. Stress tensor τ_{ij} can be written using Boussinesq's isotropic eddy viscosity hypothesis as follows.

$$\tau_{ij} = \nu_e(\frac{\partial u_i}{\partial x_j} + \frac{\partial u_j}{\partial x_i}) - \frac{2}{3}\delta_{ij}k \tag{3}$$

Here, k is turbulent kinetic energy and ν_e is effective viscosity, i.e., the sum of turbulent eddy viscosity (ν_t) and molecular kinematic viscosity (ν).

$$\nu_e = \nu_t + \frac{1}{R_e} \tag{4}$$

R_e is Reynolds number($\frac{VL_{pp}}{\nu}$). For turbulence closure, three k-ϵ models are utilized. Those are the standard k-ϵ model(hereafter SKE)(Launder and Spalding 1974), the RNG-based k-ϵ model(RNG)(Yakhot et al 1992), and the realizable k-ϵ model(RKE)(Shih et al 1995). With the k-ϵ two-equation turbulence model, the eddy viscosity ν_t can be written as

$$\nu_t = C_\mu \frac{k^2}{\epsilon} \tag{5}$$

In the standard k-ϵ model(SKE) $C_\mu = 0.09$, while in the RNG-based model(RNG) $C_\mu = 0.085$. For the Realizable k-ϵ model(RKE) C_μ has a rather complicated form given in the followings.

$$C_\mu = \frac{1}{A_o + A_s \frac{U^* k}{\epsilon}}$$

where the terms are defined as

$$\begin{aligned}
U^* &= \sqrt{S_{ij}S_{ij} + \Omega_{ij}\Omega_{ij}}, \\
S_{ij} &= \frac{1}{2}\left(\frac{\partial u_i}{\partial x_j} + \frac{\partial u_j}{\partial x_i}\right), \\
\Omega_{ij} &= \frac{1}{2}\left(\frac{\partial u_i}{\partial x_j} - \frac{\partial u_j}{\partial x_i}\right), \\
A_o &= 4.0, \quad A_s = \sqrt{6}\cos\phi, \\
\phi &= \frac{1}{3}\arccos(\sqrt{6}W), \\
W &= \frac{S_{ij}S_{jk}S_{ki}}{\tilde{S}^3}, \quad \tilde{S} = \sqrt{S_{ij}S_{ij}}
\end{aligned}$$

Turbulent kinetic energy k can be obtained by the solution of the following transport equation. For all three k-ϵ models, equation for k has the same form as given by

<u>Turbulent kinetic energy transport equation</u>

$$\frac{\partial k}{\partial t} + \frac{\partial (u_j k)}{\partial x_j} = \frac{\partial}{\partial x_j}\left\{(\nu + \frac{\nu_t}{\sigma_k})\frac{\partial k}{\partial x_j}\right\} + G - \epsilon \tag{6}$$

where ϵ represents the dissipation rate of turbulent kinetic energy and G is production term as given below.

$$G = \nu_t \left(\frac{\partial u_i}{\partial x_j} + \frac{\partial u_j}{\partial x_i}\right)\frac{\partial u_i}{\partial x_j} \tag{7}$$

In the standard k-ϵ model(SKE) and the Realizable k-ϵ model(RKE), $\sigma_k = 1.0$, while in the RNG-based model(RNG) $\sigma_k = 0.719$. Transport equation for dissipation rate ϵ is written by

Dissipation of turbulent energy equation

$$\frac{\partial \epsilon}{\partial t} + \frac{\partial (u_j \epsilon)}{\partial x_j} = \frac{\partial}{\partial x_j}\left\{(\nu + \frac{\nu_t}{\sigma_\epsilon})\frac{\partial \epsilon}{\partial x_j}\right\} + S_\epsilon \tag{8}$$

In SKE and RNG,

$$S_\epsilon = C_{\epsilon 1}\frac{\epsilon}{k}G - C_{\epsilon 2}\frac{\epsilon^2}{k}$$

where for SKE, $\sigma_\epsilon = 1.3, C_{\epsilon 1} = 1.44$, and $C_{\epsilon 2} = 1.92$. While for RNG, $\sigma_\epsilon = 0.719, C_{\epsilon 1} = 1.42$, and $C_{\epsilon 2}$ is given by

$$C_{\epsilon 2} = 1.68 + \frac{C_\mu \eta^3 (1 - \eta/4.38)}{1 + 0.012\eta^3}, \quad \eta = S\frac{k}{\epsilon}, \quad S = \sqrt{2S_{ij}S_{ij}}.$$

In RKE,

$$S_\epsilon = C_{\epsilon 1} S\epsilon - C_{\epsilon 2}\frac{\epsilon^2}{k + \sqrt{\nu\epsilon}}, \ \sigma_\epsilon = 1.2, \ C_{\epsilon 2} = 1.9, \text{ and } C_{\epsilon 1} = \max[0.43, \frac{\eta}{\eta + 5}].$$

It is advisory to use a near-wall turbulence model to resolve boundary layer up to the wall, however, it will require usually twice of grids. For the present study the so-called Launder and Spalding's wall function(Van et al 1998) is utilized to bridge the fully turbulent region and the wall. The first grid point in the wall function approach is approximately 100 times off the wall compared to that in the near wall turbulence model. It provides the economy and robustness for CFD tools. Since the flows around a ship of the present interest, the so-called singular separation with back flow is not expected, although the formation of longitudinal vortices is often observed. The wall function is known to give good results for such a mild flow. The wall function adopted in the present calculation is given by

Launder and Spalding's wall function

$$\frac{U_P C_\mu^{1/4} k_P^{1/2}}{\tau_w} = \frac{1}{\kappa}\ln(E n_P^*), \ \kappa = 0.41, \ E = 8.342 \tag{9}$$

where τ_w is wall shear stress, U_P and k_P are the magnitude of velocity and turbulent kinetic energy at the center of the first cell off the wall. The non-dimensionalized normal distance from the wall n_P^* is given by

$$n_P^* = \frac{C_\mu^{1/4} k_P^{1/2} n_P}{\nu}.$$

Generation of turbulent kinetic energy at the first cell off the wall is given as follows.

$$\overline{G_P} = \tau_w(\frac{\partial U}{\partial n})_P = \frac{\tau_w^2}{\kappa C_\mu^{1/4} k_P^{1/2} n_p}$$

while dissipation at that cell is written by

$$\overline{\epsilon_P} = \frac{C_\mu^{3/4} k_P^{3/2}}{\kappa n_p}$$

4 Grid Generation

To make it easier to apply the CFD to calculating turbulent flow around a practical hull form such as the present VLCC hull form, an efficient pre-processor is developed for surface and field grid generation(Shih et al 1995). A hull surface mesh generating program based on given station offsets along with stern and bow profiles has been developed. This new method employs non-uniform parametric splines with predetermined waterline end-shapes of natural spline, normal spline, ellipse, parabola, hyperbola, and their combinations. It takes less than ten minutes in PC to obtain hull surface meshes, starting from a given offset table. Mesh topology chosen in the present study, to present hull surface with bulbous bow and stern end bulb, can be transformed into a rectangle. It implies that flow solvers are able to accommodate the mesh easily and their own accuracy does not deteriorate especially when turbulent quantities are determined by the so-called wall coordinate. The generated hull surface meshes can be used immediately as boundary surface grids for field grid generation Utilizing the generated surface meshes, Poisson equation is solved to constitute the field grid system of O-O topology. In the present study outer boundary surface resembles a bullet, where appropriate boundary conditions are easily identified. Sorenson's method(Sorenson 1980) is extended into three-dimensional one to specify grid-control functions. Weighted trans-finite interpolation is also utilized to specify the better initial guess and to make smooth transition of 3D grids into 2D boundary grids(Kim et al 1998). Fig.3 shows obtained grid system for turbulent flow calculation around a VLCC hull form. Surface meshes near bow and stern are well fitted with profiles of the ship. Since the present calculation employs the so-called wall function approaches, the distance of the first grid point off the wall is around 0.5×10^{-3}. For the present calculation, three grid systems of $81 \times 29 \times 25, 97 \times 33 \times 33$, and $113 \times 37 \times 41$ grids are generated to investigate grid dependence of the solution. The calculated radial distribution of circumferentially averaged axial velocity components at propeller plane, which is the most important information for propeller design, is compared when the realizable k-ϵ model is utilized. ¿From Fig.4, it is clear that $97 \times 33 \times 33$ grids are sufficient for the practical applications. From now on, all calculated results shown in the paper are obtained with $97 \times 33 \times 33$ grids.

5 Numerical Methods

The cell-centered finite-volume method is utilized to discretized governing equations, as discussed in Ferziger and Peric(1996). Governing equations are integrated over a grid cell Ω with boundary surface S, resulting in the following equations.

$$\int_S \vec{v} \cdot \vec{n} dS = 0$$

$$\frac{\partial}{\partial t} \int_\Omega u_i d\Omega + \int_S u_i \, \vec{v} \cdot \vec{n} dS = \int_S \tau_{ij} \, \vec{i}_j \cdot \vec{n} dS - \int_S p \, \vec{i}_i \cdot \vec{n} dS$$

where $\vec{i}_j$ is unit vector in x_j direction. The first term of momentum transport equation, temporal derivative is ignored by putting very big time step, since only the steady solution is of the present interest. Convection terms are discretized using QUICK scheme of the third order. But the QUICK scheme requires 13 point stencil, resulting in complicated algebraic equations. Thus, the so-called deferred correction approach is adopted, which a simple upwind scheme is used with lagged higher order terms. The deferred correction makes 7 point stencil with simple linear equations. Rewriting the third term of stress tensor,

$$\int_S \tau_{ij} \, \vec{i}_j \cdot \vec{n} dS = \int_S \nu_t (\frac{\partial u_i}{\partial x_j} + \frac{\partial u_j}{\partial x_i}) \vec{i}_j \cdot \vec{n} dS = \int_S \nu_t (\text{grad}(u_i) \cdot \vec{n} + \frac{\partial u_j}{\partial x_i} \vec{i}_j \cdot \vec{n}) dS$$

where the term with turbulent kinetic energy is included in pressure gradient. Central difference scheme is utilized for diffusion terms, while the terms coming from grid non-orthogonality is deferred. Linear equations obtained from 7 point stencil are solved using strongly implicit procedure(Stone 1968). If the pressure field is known a prior, momentum equations will give correct velocity field. However, those velocity components will not satisfy the continuity equation. To ensure divergence-free velocity field, the SIMPLEC method(Van Doormal and Raithby 1984) is employed. Since the collocated grid arrangement is chosen, the artificial dissipation term in pressure correction equation is added, as discussed in Rhie and Chow(Rhie and Chow 1983). As mentioned in the above momentum equation, pressure correction equation also have the terms related to grid skewness. In the present study, as recommended in Ferziger and Peric(1996), the second correction is added to compensate for deferred correction terms in pressure correction equation. Again, the resulting linear equations are solved using strongly implicit procedure until the equation residual drops by an order of magnitude each iteration. To complete the solution procedures, at first, hull surface meshes are generated as mentioned earlier. Taking the generated surface as a boundary surface, three-dimensional field grids are obtained. With the generated grid system, flow calculation is initiated, starting from uniform stream (i.e., abrupt start). With the grids and initial guess for flow field ready, iteration begins for coupled partial differential equations. After three momentum transport equations are solved sequentially to obtain preliminary velocity components, pressure correction equations is solved to get pressure field. Then, velocity components are corrected using new pressure field. In the next turbulence equations are solved and eddy viscosity is updated. Iteration continues until total residuals of each momentum equation are less than 10^{-5}, which is about five order less than the initial residuals.

6 Results and Discussion

In the followings the calculated results are compared with experiments. At first, for KVLCC, the results with three different turbulence models are discussed to investigate the effect of turbulence

model on flow prediction. In the next, propeller plane wakes are investigated carefully for two hull forms with stern frameline modification to see that the present computational modelling can identify the difference of stern hull form quantitatively as well as qualitatively. It should be noted that the measurements were carried out in towing tank, thus, flow field was certainly affected by wave generation on the free surface. However, the present calculation ignores the effect of waves, since wave generation of the VLCC is not significant because of low Froude number. Instead, Neumann condition is applied on the calm free surface. In Figs. 5~7, calculated velocity fields with SKE, RNG, and RKE are compared to experiments at station 2 and 0.35. The calculated results with SKE shows thicker boundary layer at station 2, while little bilge vortices are found at the propeller plane. For RNG, boundary layer thickness are predicted better, however, the RNG-based k-ϵ model still failed to predict distortion of axial velocity contours at the propeller plane. On the other hand, the realizable k-ϵ model(RKE) provides correct boundary layer thickness with hook-like distortion of axial velocity contours. It is rather surprising, since the wall function is utilized to skip the details of near wall turbulence phenomena. In Fig.8 propeller plane wakes are compared. As expected from Figs. 5 and 6, SKE and RNG failed to predict the hook in U-contours, while RKE succeeded. The sharp turning of wake contours around lower part of 0.4R is observed, which is believed to come from the numerical method or grid topography. Calculated turbulent kinetic energy and eddy viscosity are shown in Fig.9 and 10. RNG provided lower level of turbulence than the others. Eddy viscosity contours of SKE and RNG show similar shapes, as expected from the axial velocity contours. RKE has lower eddy viscosity values than SKE and RNG except at the location above hub and near vortex core, where high eddy viscosity is concentrated. These figures might give some clues on that RKE gives nice hook-like shape as in Fig.8. It is noteworthy that coefficient C_μ in Eq. 5 of RKE is not a constant but a function of mean strain rate and vorticity, and the contours of C_μ in RKE resembles those of eddy viscosity. It would be premature to tell which turbulence model is superior in predicting wake distribution, but RKE seems to have an edge. In practical application of viscous flow calculation to design of commercial ships, the most common usage will be to provide nominal wake distribution for propeller design in advance. Fig.11 shows radial distribution of circumferentially averaged axial velocity components at propeller plane of KVLCC and KVLCC2. As already shown in Fig.8, SKE shows poor results for both ship. The RNG-based k-ϵ model(RNG) gives a little better results, but still far from the experiment. However, the realizable k-ϵ model(RKE) yields to fairly good agreement with experiments for both ships. The discrepancy near hub (0.3~0.4R) might be coming from the simple extrapolation of velocity fields of the experiment, since the measured local flow angles are out of calibration range beneath the hub, thus, thus, discarded in the experiment. If the velocity distribution outside of 0.5R is considered, RKE gives directly applicable results, which is very encouraging. The answer for question that the present computational modeling can tell the difference of stern frameline modification will be addressed later. Calculated surface pressure distribution and surface friction lines are demonstrated in Fig.12 and 13 for KVLCC with RKE model. The calculated pressure around the bow bulb of KVLCC migrate smoothly into low pressure region around a bow shoulder. Pressure gradient in diagonal direction is seen which is also the direction of limiting streamlines. Since the bulb of the VLCC is relatively small, pressure change across the bulb is not so radical as ships with long bulb, e.g., container ships. Low pressure region near the bottom bilge is also observed. The pressure variations near the stern of both hull forms are much milder than near the bow region, since thick boundary layer near the stern prohibits the rapid change of pressure field. The flow patterns from bow bulb to midship can be considered mainly

as a potential flow with thin boundary layer. However, as focus moves downstream towards stern, thick boundary layer and wake flows developed along the streamlines will clearly demonstrate the effect of turbulence in viscous flow. The formation of stern bilge vortices are clearly seen in Fig.13. Surface friction lines are converged near the stern bilge, which is shown as a thick line. In the next, measured and calculated wake distribution for KVLCC and KVLCC2 will be discussed. As mentioned earlier KVLCC2 has been modified to fortify bilge vortices, which is clearly seen in Fig. 14-(a). KVLCC2 has stronger hook-like U-contours. All three turbulence models make some difference in wakes, although those of SKE and RNG are quite different from the experiment. RKE provides very reasonable difference between KVLCC and KVLCC2. To see the difference between KVLCC and KVLCC2, circumferentially averaged axial velocity distributions are shown in Fig.15. Surprisingly all three models give almost the same amount of difference between the two ships, except near hub. This observation probably makes CFD applicants of ship yards happy. If the viscous calculation was used only for the qualitative purpose, SKE with wall function should have given the right answer, although the values are not in agreement with the experiment. The other point from the present calculation is that calculated wake distribution with the realizable k-ϵ model(RKE) gives fairly good agreement with the experiment. One of the conclusion drawn from the present computation is that it is possible to predict nominal wake distribution in pretty good accuracy with RKE and wall function. Surface pressure and friction lines on KVLCC and KVLCC2 with RKE is shown in Fig.16. There is little difference in pressure, however, this difference will make some difference in viscous pressure drag, since normal vectors near the stern region will affect the pressure drag. Limiting streamlines of KVLCC2 near the stern region shows a little stronger convergence into open separation line than in KVLCC, but difference is not very notable. However, it should be mentioned here that this amount of change is usually applied in ship yards for hull form improvement. Finally integrated parameters are compared in Table 2. Surface friction coefficients of KVLCC and KVLCC2 with the same turbulence model are very similar, while a little of difference is found between the turbulence models. However, there are bigger difference in viscous pressure drag coefficients and nominal wake. SKE again failed to predict the pressure drag. RKE are the closest, since the wave making resistance coefficient of the present VLCCs at the Froude number of 0.142 is about 0.15×10^{-3}. In nominal wake prediction, as noted earlier, RKE gives pretty close values to the experiment. With $97 \times 33 \times 33$ grids, the computing time was around 1.5 hours in SGI Onyx 2 (344 MFLOPS). It is believed that hull form designers can get the viscous flow solution in engineering workstations within working hours, starting from the station offset table.

7 Concluding Remarks

In order to confirm that the viscous flow calculation with affordable difficulties can predict nominal wake distribution correctly, flow calculations are performed for the two modern practical VLCCs with the same forebody and the slightly different afterbody, i.e., KVLCC and KVLCC2. The focus is laid upon the application of relatively simple computational modeling to provide the enough information to hull form designers, when they really modify hull forms in ship yards. The Reynolds-averaged Navier-Stokes equations for turbulent flows around model ships are solved using the cell-centered finite-volume schemes. Several variations of two-equation turbulence models, such as the standard k-ϵ model(SKE), the RNG-based k-ϵ model(RNG), and the realizable

Table 2: Resistance coefficients and nominal wakes

	300K VLCC F1+A1 (KVLCC)				300K VLCC F1+A2 (KVLCC2)			
Turbuelnce model	Exp	SKE	RNG	RKE	Exp	SKE	RNG	RKE
Reynolds Number	4.6×10^6				4.6×10^6			
$C_F \times 10^3$	3.450*	3.694	3.431	3.346	3.450*	3.697	3.433	3.351
$C_{VP} \times 10^3$	0.638*	0.908	0.312	0.481	0.660*	0.944	0.347	0.524
Nominal wake	0.523	0.387	0.417	0.503	0.561	0.450	0.484	0.556

* C_F and C_R based on 1957 ITTC formula(experiments with rudder in free condition)

k-ϵ model(RKE), with Launder and Spalding's wall function are tested to identify the differences caused by the turbulence models. The calculated results around the two VLCC hull forms using O-O grid topology and profile-fitted surface meshes are compared to the measured data from towing tank experiment. It is observed that the realizable k-ϵ model(RKE) provided realistic wake distribution with hook-like shape, while other two models failed. Furthermore, it is found that simple turbulence modeling is still effective to use for hull form evaluation purpose, since the predicted values in resistance coefficients and nominal wake fractions are in good agreement to the experiment if the proper turbulence model is chosen. It is very encouraging to see that the CFD with relatively simple turbulence closure can tell the difference quantitatively as well as qualitatively for the two hull forms with stern frameline modification.

Acknowledgement

The present work is based on the projects of "Improvement of Resistance Performance of Ships," supported by Ministry of Industry and Resources, and "Development of Hydrodynamic Performance Analysis System," supported by Ministry of Science and Technology. Turbulent flow calculations are performed in SGI Onyx 2 (R10000 CPU, 195 MHz).

References

CFD WORKSHOP TOKYO 1994 Proc. of CFD Workshop Tokyo- an international workshop for improvement of hull form designs, Tokyo, Japan

FERZIGER, J.H. AND PERIC, M. 1980 Computational Methods for Fluid Dynamics, Springer-Verlag

HIMENO, Y. ET AL 1998 Proc. of Osaka Colloquium on advanced application of CFD on hull form design, Osaka, Japan

KIM, S.E. ET AL 1998 A Reynolds-averaged Navier-Stokes solver using unstructured mesh-based finite-volume scheme. AIAA 98-0231

KIM, W.J. ET AL 1980 Computational study on turbulent flow around practical hull forms with efficient grid generator. Proc. of Osaka Colloquium on advanced application of CFD on hull form design, Osaka, Japan

LARSSON, L., PATEL, V.C. AND DYNE, G. 1991 Ship Viscous Flow. Proc. of SSPA-CTH-IIHR WORKSHOP. Gothenburg, Sweden

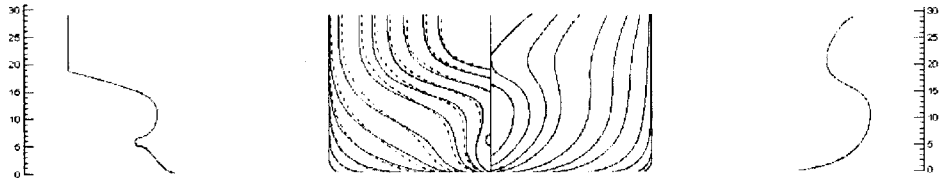

Figure 1: Body plans & side profiles of 300K VLCC(solid: A1, dashed: A2)

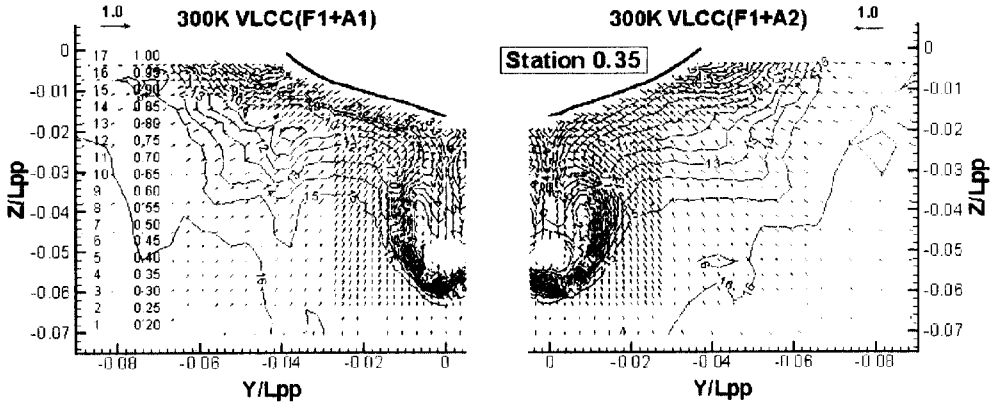

Figure 2: Measured velocity fields of KVLCC and KVLCC2 at St. 0.35

LAUNDER, B.E. AND SPALDING, D.B. 1974 The Numerical Computation of Turbulent Flows. Comp. Meth. Appl. Mech. Eng., **3**, pp. 269-289

RHIE, C.M. AND CHOW, W.L. 1983 A Numerical Study of Turbulent Flow Past an Isolated Airfoil with Trailing Edge Separation. AIAA Journal, **21**, pp. 307-357

SHIH, T.H., LIOU, W.W., SHABIR, A. AND ZHU, J. 1995 A New k-ϵ Eddy Viscosity Model for High Reynolds Number Turbulent Flows-Model Development and Validation. Computers and Fluids, **24**, **3**, pp. 227-238

SORENSON, R.L. 1980 A computer program to generate two-dimensional grids about airfoils and other shapes by the use of Poisson equation. NASA TM 81198

STONE, H.L. 1968 Iterative Solution of Implicit Approximations of Multi-directional Partial Differential Equations. SIAM J. of Numer. Anal., **5**, pp. 530-558

VAN DOORMAL, J.P. AND RAITHBY, G.D. 1984 Enhancements of the SIMPLE method for Predicting Incompressible Fluid Flows. Numerical Heat Transfer, **7**, pp. 147-163

VAN, S.H. ET AL 1998 Experimental study on the flow characteristics around VLCC with different stern shapes. Proc. of the Third International Conference on Hydrodynamics(ICHD), Seoul, Korea

YAKHOT, V., ORSZAG, S.A., THANGAM, S., GATSKI, T.B. AND SPEZIALE, C.G. 1992 Development of turbulence models for shear flows by a double expansion technique. Physics of Fluids A, **4**, **7**, pp. 1510-1520

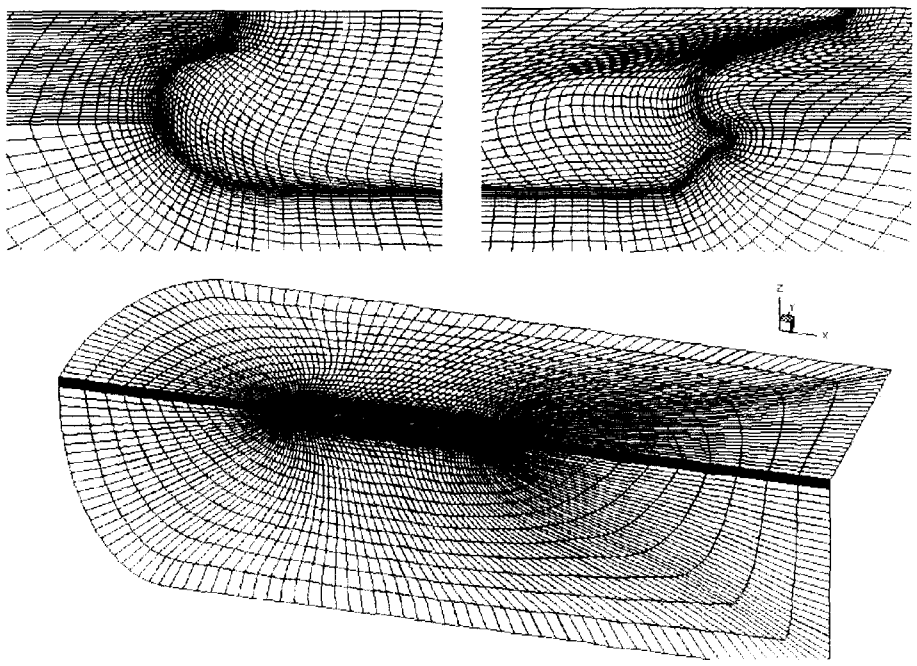

Figure 3: Grid system of O-O topology

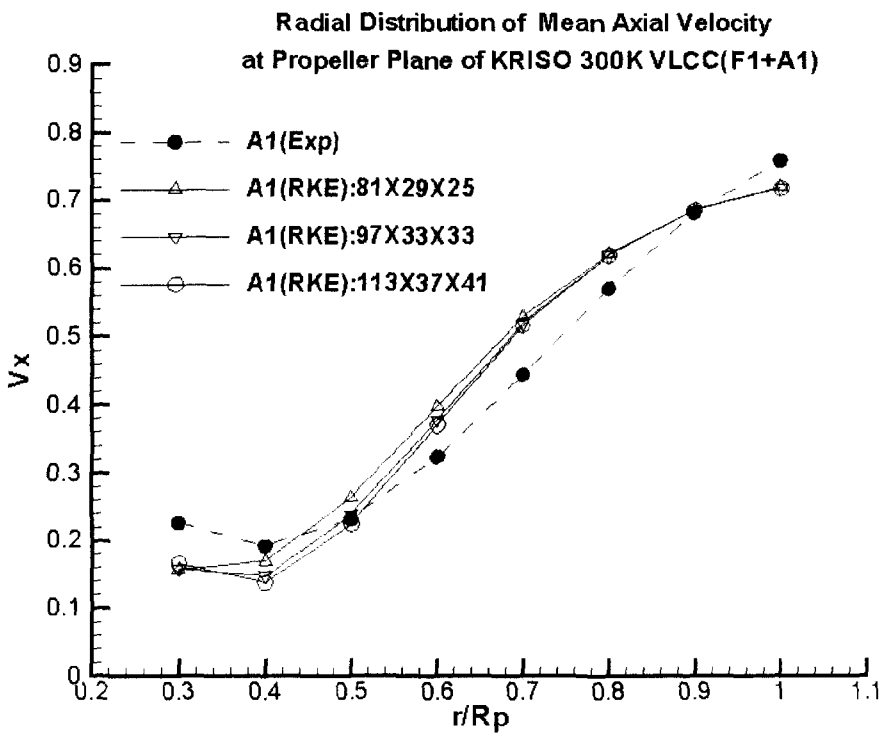

Figure 4: Wake distribution with 3 grid levels

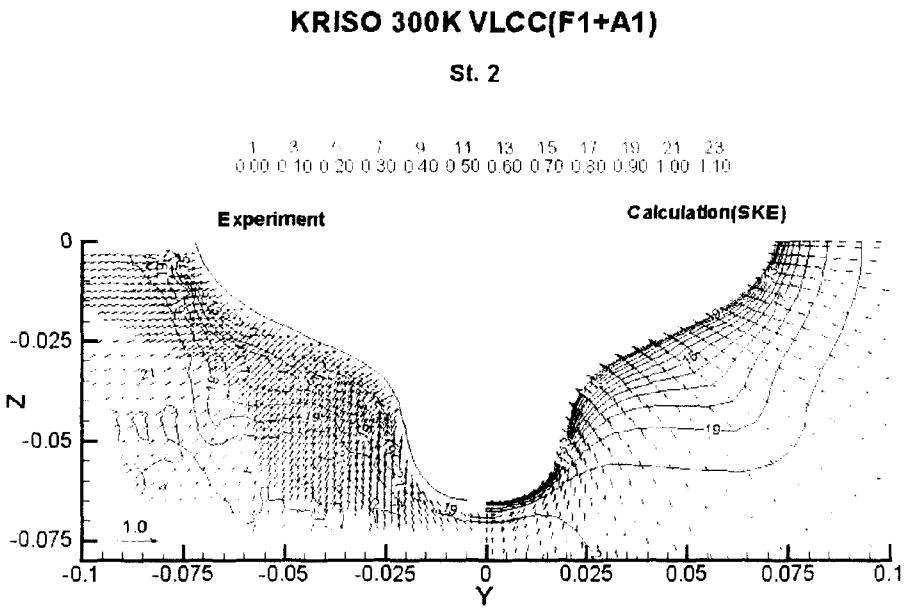

(a) St. 2

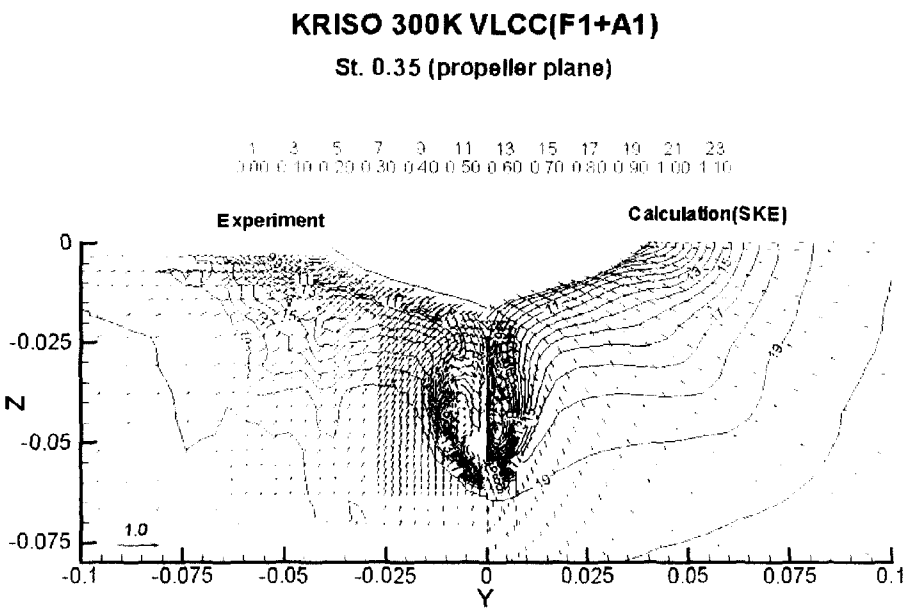

(b) St. 0.35

Figure 5: Comparison of velocity fields(KVLCC) with the standard $k-\epsilon$ model(SKE)

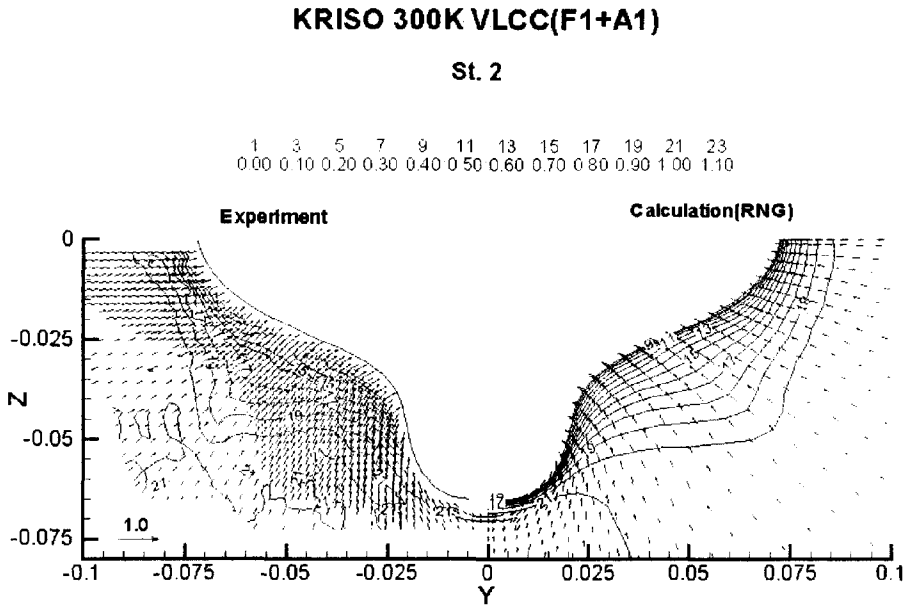

(a) St. 2

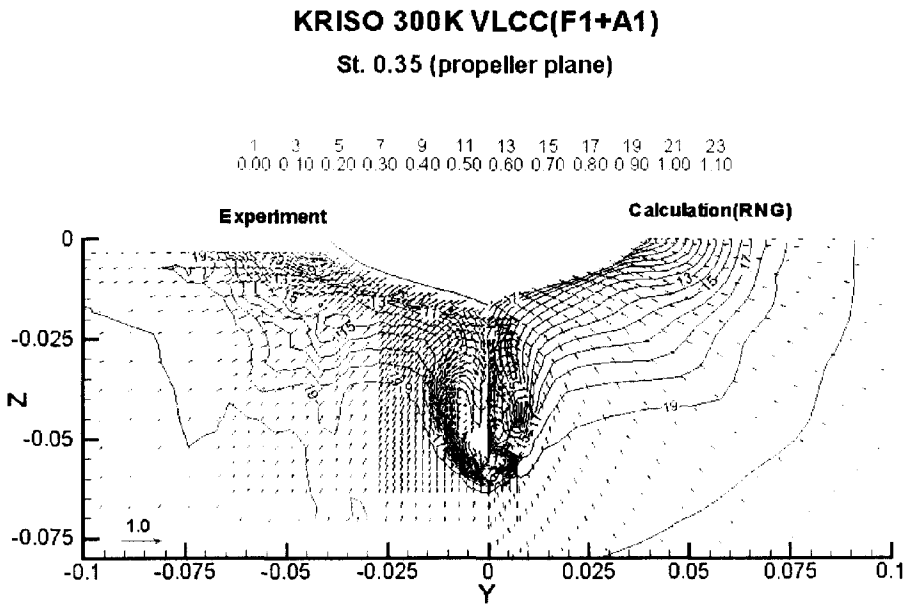

(b) St. 0.35

Figure 6: Comparison of velocity fields(KVLCC) with the RNG-based $k-\epsilon$ model(RNG)

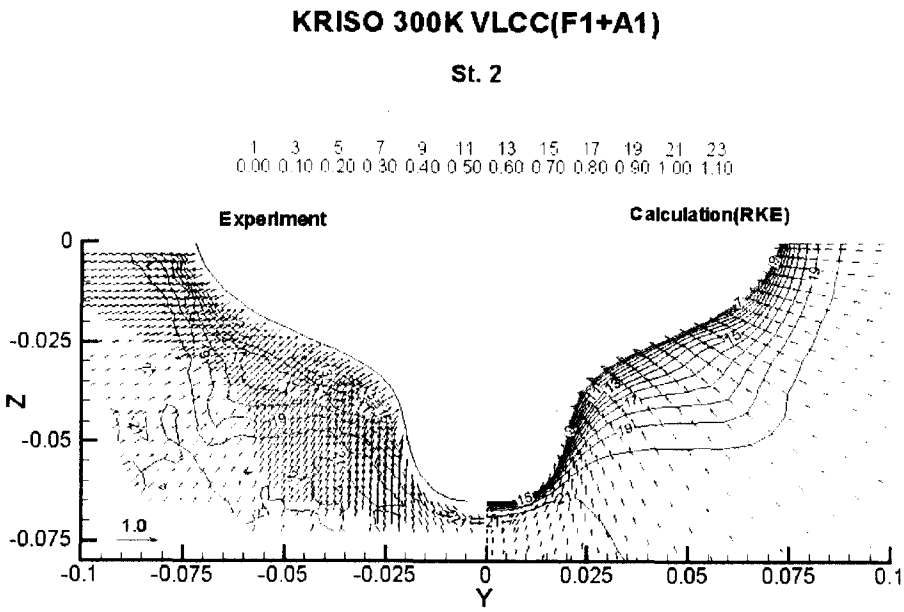

(a) St. 2

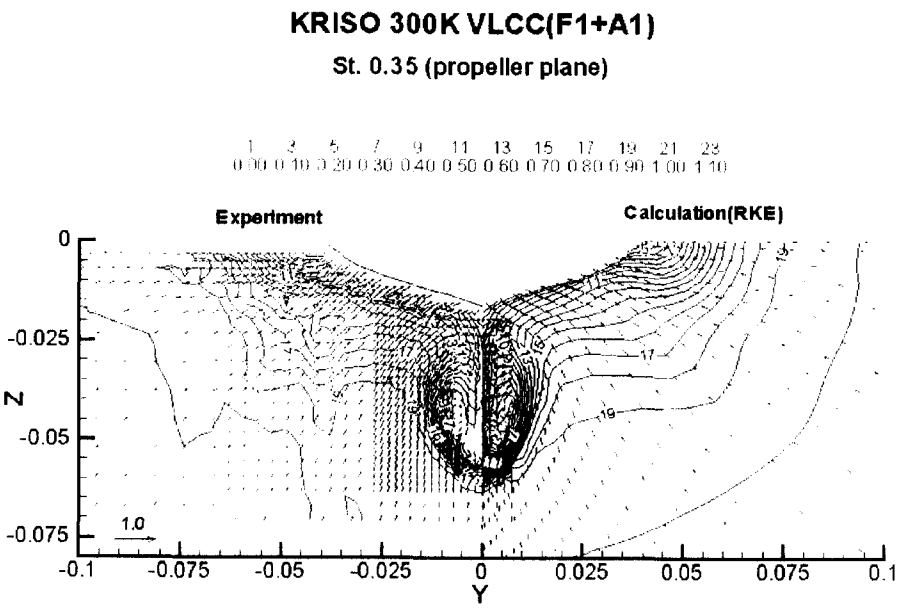

(b) St. 0.35

Figure 7: Comparison of velocity fields(KVLCC) with the realizable $k-\epsilon$ model(RKE)

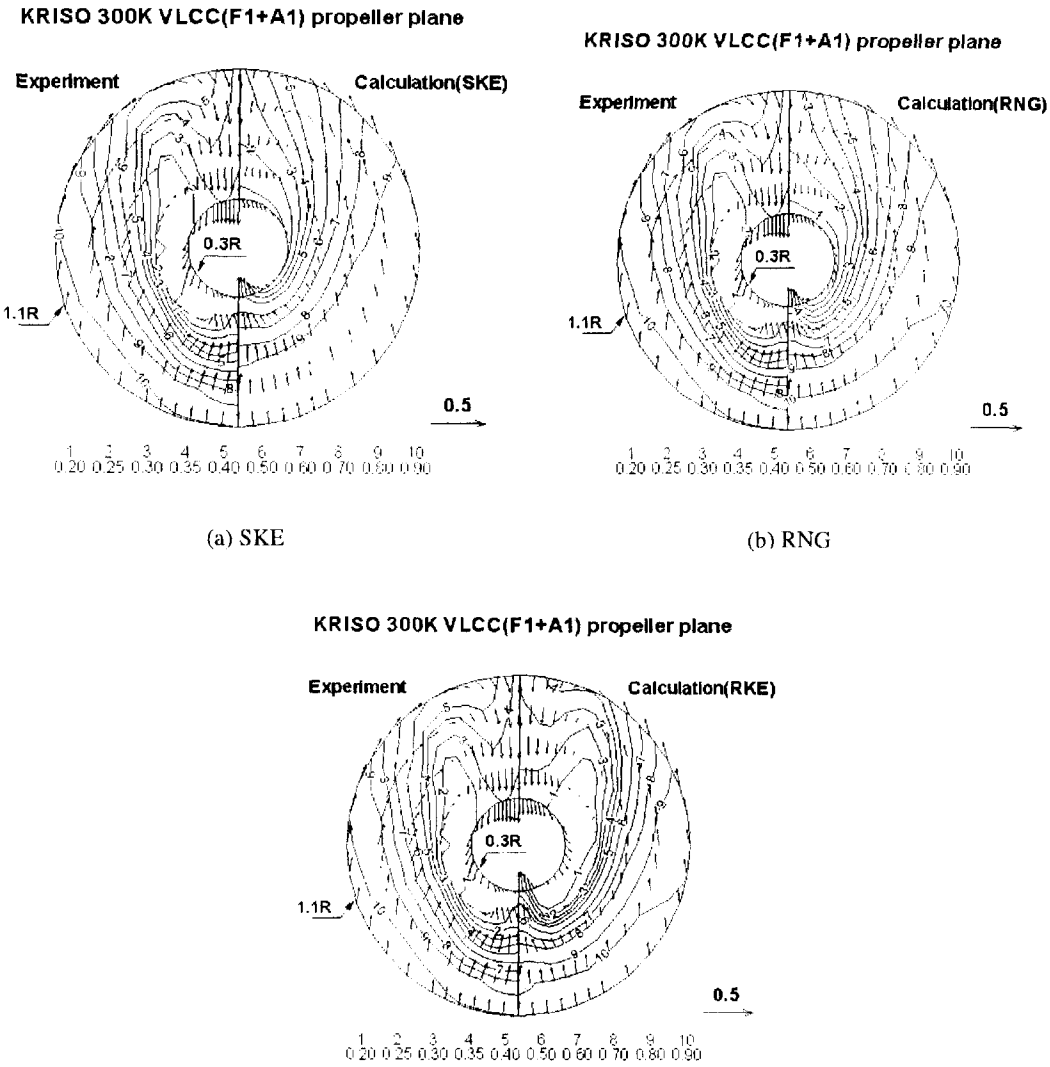

(a) SKE

(b) RNG

(c) RKE

Figure 8: Extracted velocity fields(KVLCC) at the propeller plane

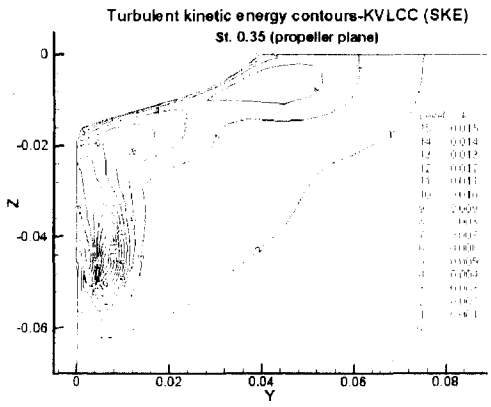

(a) SKE

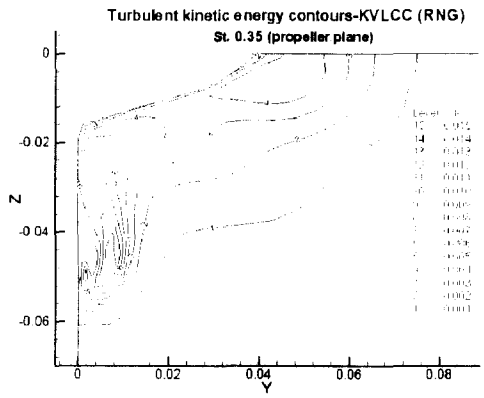

(b) RNG

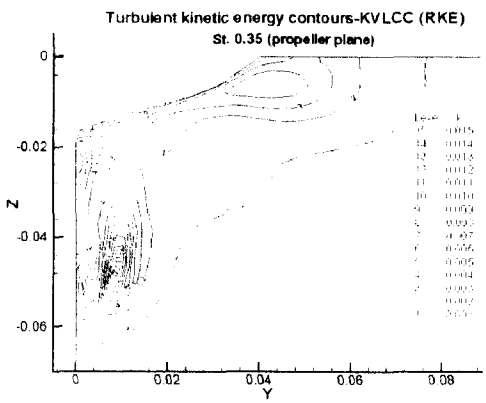

(c) RKE

Figure 9: Calculated turbulent kinetic energy contours at the propeller plane

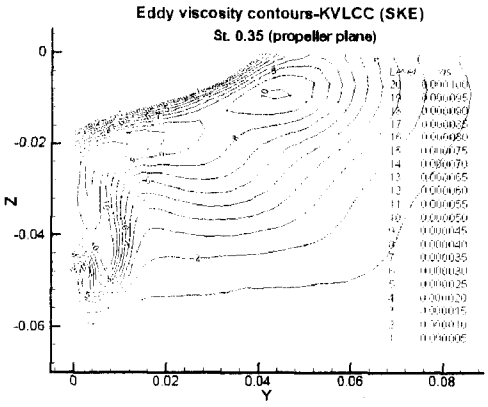

(a) SKE

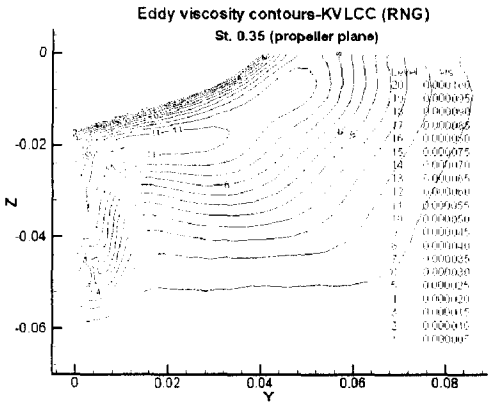

(b) RNG

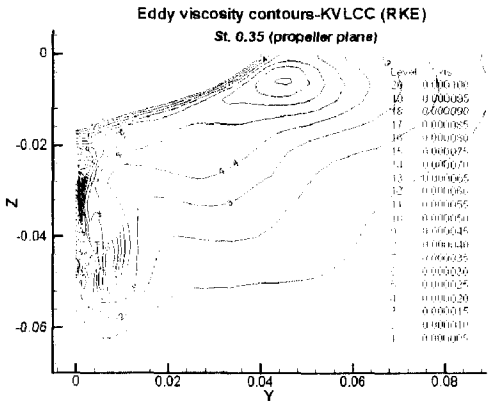

(c) RKE

Figure 10: Calculated eddy viscosity contours at the propeller plane

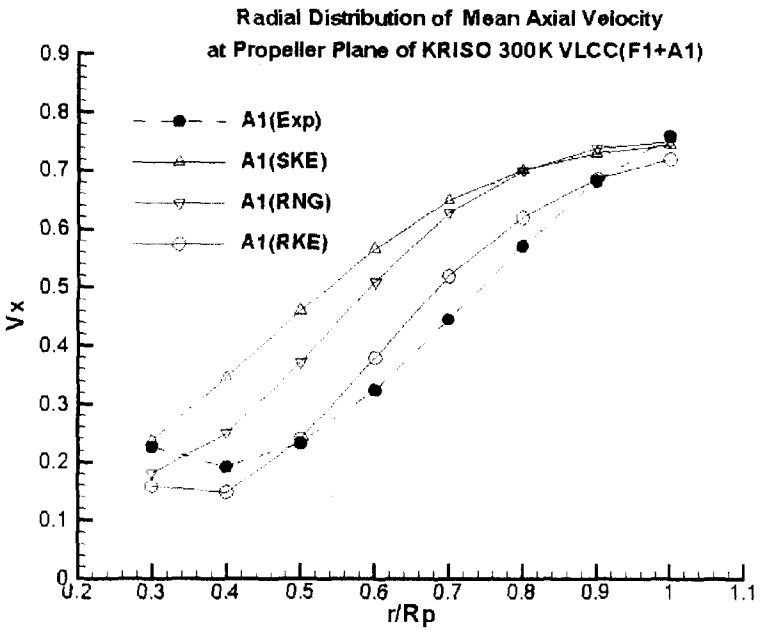

(a) KVLCC

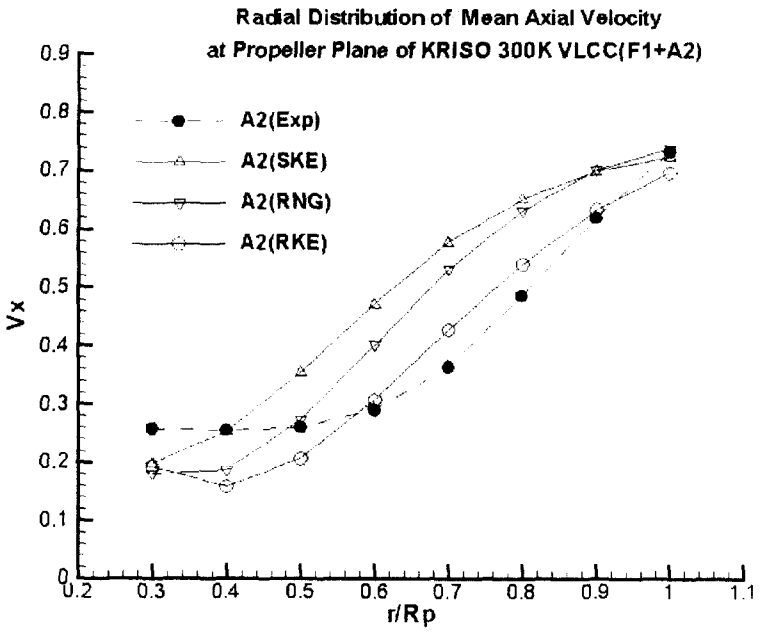

(b) KVLCC2

Figure 11: Radial distribution of circumferentially averaged axial velocity components at the pro peller plane of KVLCC and KVLCC2

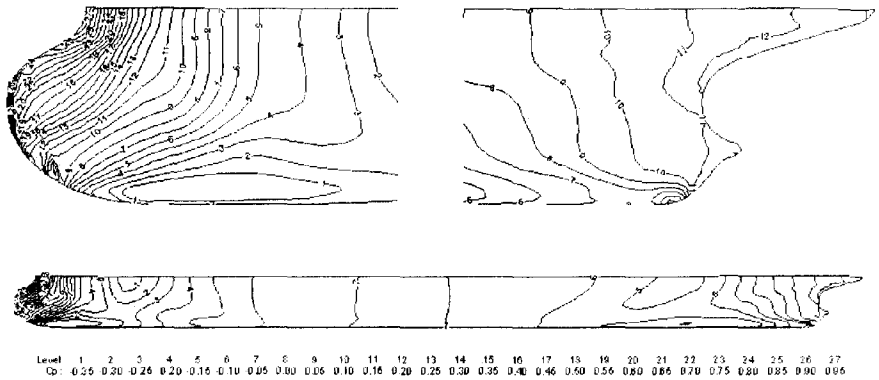

Figure 12: Calculated surface pressure distribution of KVLCC with the realizable $k - \epsilon$ models

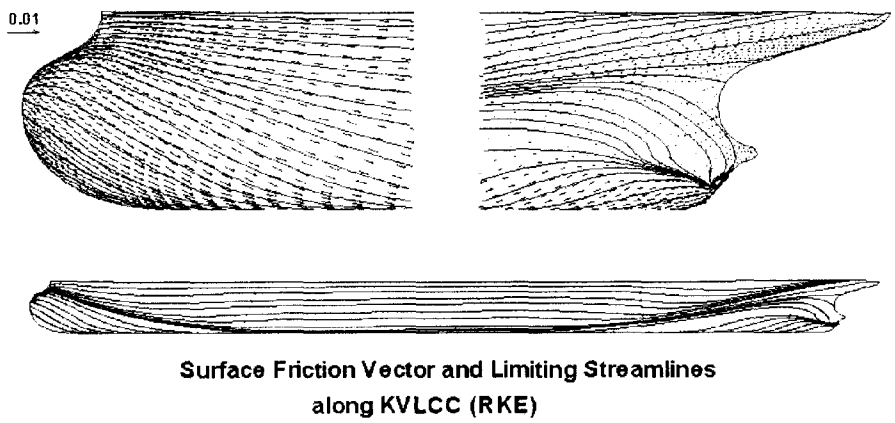

Figure 13: Calculated friction vectors and limiting streamlines on KVLCC with the realizable $k - \epsilon$ models

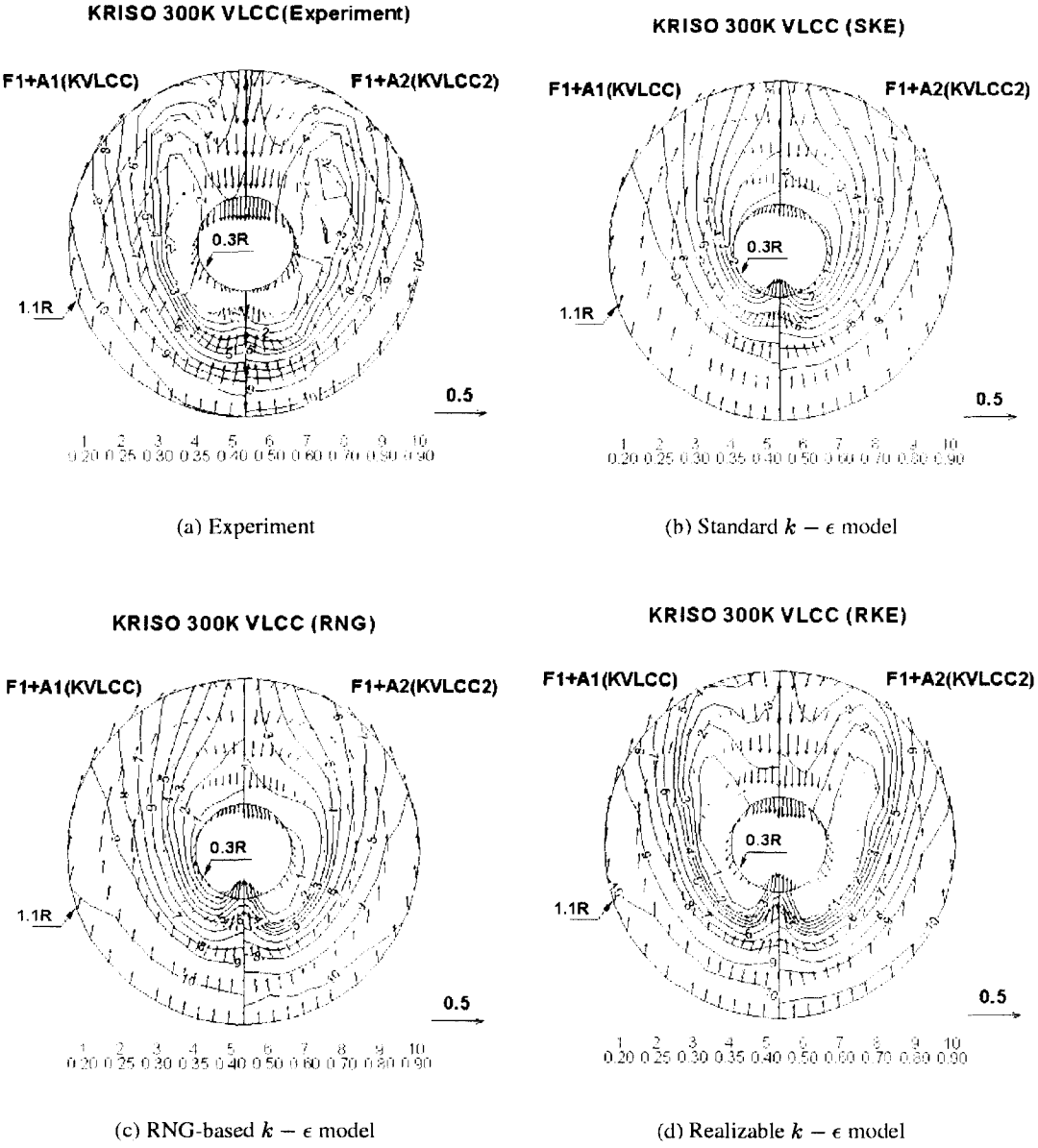

(a) Experiment

(b) Standard $k - \epsilon$ model

(c) RNG-based $k - \epsilon$ model

(d) Realizable $k - \epsilon$ model

Figure 14: Comparison of wake distribution of KVLCC and KVLCC2 at the propeller plane

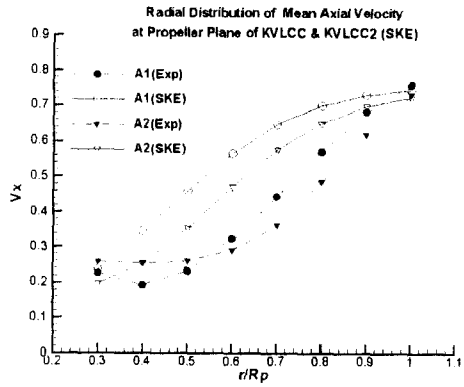

(a) SKE

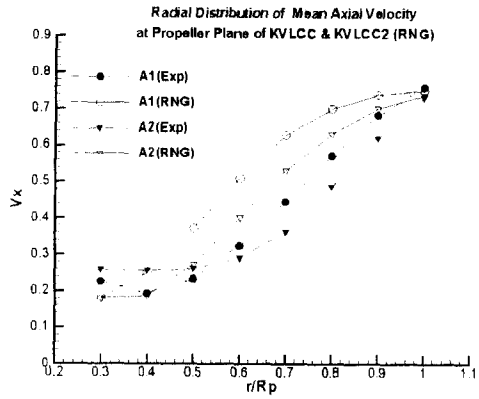

(b) RNG

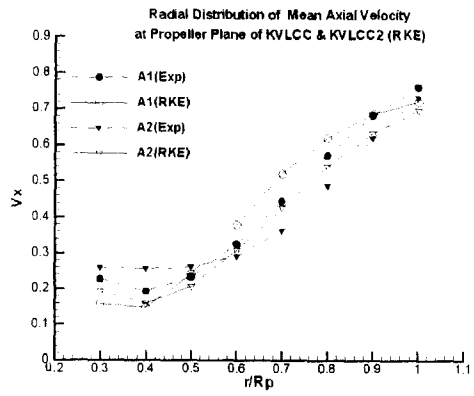

(c) RKE

Figure 15: Comparison of circumferentially averaged axial velocity distribution of KVLCC and KVLCC2 at the propeller plane with three $k - \epsilon$ models

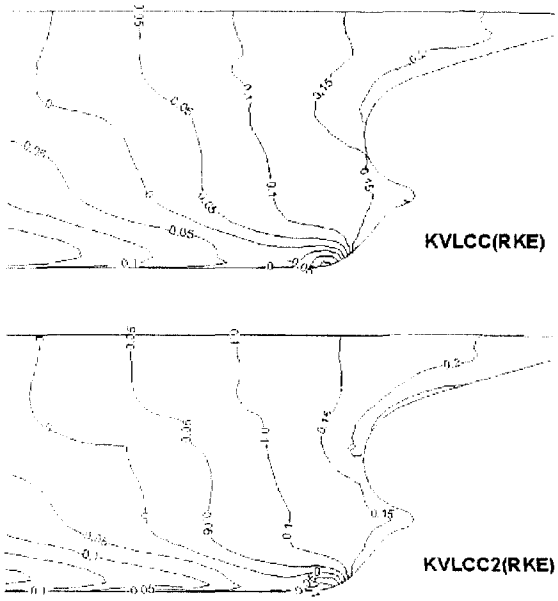

(a) Surface pressure

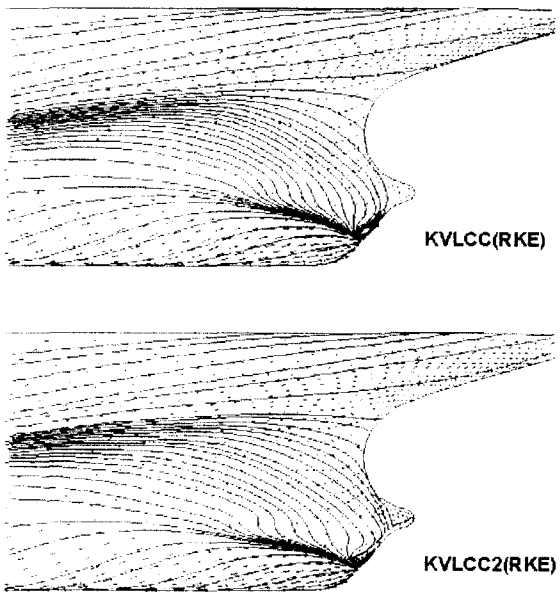

(b) Limiting streamlines

Figure 16: Calculated surface pressure and friction lines on KVLCC and KVLCC2 with the realizable $k - \epsilon$ model(RKE)